Article

13.2% Efficiency of Organic Solar Cells by Controlling Interfacial Resistance Resulting from Well-Distributed Vertical Phase Separation

Hee Seon Park, Yong Woon Han, Hyoung Seok Lee, Sung Jae Jeon, and Doo Kyung Moon*

Read Online

| ACCESS | Metrics & More | Article Recommendations | SI Supporting Information |

ABSTRACT: Two strategies were investigated to improve the efficiency of organic solar cells (OSCs) with the aim of controlling the interfacial resistance in the devices: the use of a ternary active layer and the introduction of conjugated polymers. The ternary active layer was formed by introducing $PC_{71}BM$ between a high-performance non-fullerene photoactive material P(Cl–Cl) (BDD = 0.2) and the IT-4F-based binary active layer, thereby reducing the interfacial resistance between the donor and acceptor via vertical phase separation. Furthermore, the introduction of the conjugated polymer PFN-Br created a well-dispersed separation attributable to enhancement of the interfacial contact with the active layer and simultaneous reduction of the interfacial resistance. Consequently, the synergetic effect of the ternary active layer and PFN-Br enhanced the short-circuit current density (J_{SC}) and fill factor (FF) to realize a power conversion efficiency (PCE) of 13.2%.

KEYWORDS: organic solar cells, power conversion efficiency, interfacial resistance, ternary active layer, conjugated polymers
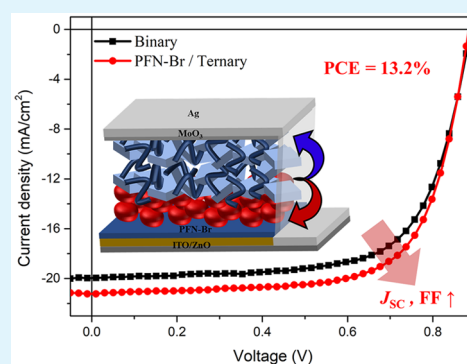
1. INTRODUCTION

Previous studies on organic solar cells (OSCs) have demonstrated that they are advantageous in several ways; for example, they are lightweight and cost-effective. Furthermore, OSCs have the potential to be used in flexible devices, they can be fabricated via a solution process, and a power conversion efficiency (PCE) of 17% or more has been reached in unit cells.[1−5] In particular, OSCs have attracted attention as next-generation energy sources that have the potential to be easily commercialized because flexible OSC modules can be manufactured through an all-solution process that is based on the roll-to-roll process.[6−11] Attempts to improve the performance capabilities of OSCs have prompted studies to investigate the effects of modifications to the molecular design of the photoactive layer and modification of device structures.[12−17]

An inverted structure, which is a typical OSC structure, comprises a stack of organic and inorganic semiconductors. The layers forming the structure consist of a transparent electrode, electron transport layers (ETLs), an active layer, hole transport layers (HTLs), and a metal electrode. The performance of OSCs can be analyzed by measuring their physical and chemical properties such as the degree and mobility of carrier movement. The resistance of the interface can be analyzed by configuring the internal interface of an OSC as one circuit because resistance is a measure of the ability of charges to move through the layers.[18−20] Consequently, it is important to enhance carrier transport by

reducing the internal resistance occurring at the interface between the different layers of an OSC circuit.[21,22] The ETLs mainly comprise inorganic semiconductors such as ZnO and TiO_x, and the active layer has a bulk-heterojunction (BHJ) composed of binary blends with an organic donor and acceptor. In this case, the domain size and morphology of the donor and acceptor in the active layer determine the interfacial resistance, resulting in carrier trapping and recombination.[18] Thus, the addition of additives such as diiodooctane (DIO) can be helpful for controlling domain size and morphology.[23,24] Moreover, the interfacial resistance increases when incompatibility at the interface between the inorganic ETLs and organic active layer causes poor contact between the layers, thereby resulting in carrier trapping and recombination.[25,26] Thus, enhancement of the process of carrier transport, which can be implemented by interfacial resistance control, is essential to obtain high-performance OSCs.

Various studies on the enhancement of carrier transport have recently been conducted. First, carrier transport can be
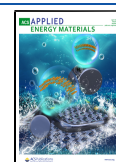
improved by including a ternary active layer in which a third component is introduced into a binary active layer. Generally, the ternary active layer is composed of one donor with two acceptors (D:A1:A2) or two donors with one acceptor (D1:D2:A), which exhibit optoelectronic properties superior to those of the binary active layer.[27] In this regard, Zhan and co-workers introduced [6,6]-phenyl C_{71} butyric acid methyl ester ($PC_{71}BM$) as the third component into a binary active layer composed of poly[(2,6-(4,8-bis(5-(2-ethylhexyl-3-fluoro)thiophen-2-yl)-benzo[1,2-b:4,5-b']dithiophene))-alt-(5,5-(1′,3′-di-2-thienyl-5′,7′-bis(2-ethylhexyl)benzo[1′,2′-c:4′,5′-c′]dithiophene-4,8-dione)] (PM6) and 2,2′-((2Z,2′Z)-((12,13-bis(2-ethylhexyl)-3,9-diundecyl-12,13-dihydro[1,2,5]-thiadiazolo[3,4-e]thieno[2″,3″:4′,5′]thieno[2′,3′:4,5]pyrrolo-[3,2-g]thieno[2′,3′:4,5]thieno[3,2-b]indole-2,10-diyl)bis-(methanylylidene))bis(5,6-difluoro-3-oxo-2,3-dihydro-1H-in-dene-2,1-diylidene))dimalononitrile (Y6) and reported an increase in carrier generation due to the formation of an effective morphology; thus, a PCE of 16.7% was achieved.[21] Furthermore, Sun and co-workers introduced poly[[4,8-bis[5-(2-ethylhexyl)-2-thienyl]benzo[1,2-b:4,5-b′]dithiophene-2,6-diyl]-2,5-thiophenediyl[5,7-bis(2-ethylhexyl)-4,8-dioxo-4H,8H-benzo[1,2-c:4,5-c′]dithiophene-1,3-diyl]] polymer (PBDB-T1), which is a donor with highly crystalline properties, into a binary active layer composed of poly[4,8-bis(5-(2-ethylhexyl)thiophen-2-yl)benzo[1,2-b:4,5-b′]-dithio-phene-co-3-fluorothieno[3,4-b]thiophene-2-carboxylate] (PTB7-Th) and $PC_{71}BM$. They reported enhanced carrier transport and dissociation improved the PCE from 8.7% to 10.2%.[28]

Second, carrier transport can also be improved by introducing conjugated polymers into the buffer layer. Shen and co-workers introduced SnO_2 and poly[(9,9-bis(3′-(N,N-dimethylamino)propyl)-2,7-fluorene)-alt-2,7-(9,9-dioctylfluor-ene)] (PFN) as a buffer layer to fabricate OSCs, and they reported that the interfacial dipoles resolved the misalignment of energy levels, resulting in a maximum PCE of 11.05%.[29]

Third, a reduction in the internal resistance of a device can decrease carrier recombination and increase carrier transport. Guo and co-workers introduced a poly(ethylenimine) (PEI)/SnO_2/PFN structure into SnO_2 ETLs, thereby reducing the interfacial resistance by establishing effective contact between the active and cathode layers, and they reported that a reduction in carrier recombination resulted in an improvement in the PCE from 5.51% to 7.18%.[30] Furthermore, an inducement of vertical phase separation in active layer can cause efficient carrier transport and drastic enhancement of performances.[31] Wei, Yang, and co-workers proved that the vertical phase separation resulted from thermodynamically changed surface properties increased PCE of devices with efficient charge extraction.[32] It would therefore be reasonable to expect that the formation of a ternary active layer in combination with the introduction of conjugated polymers would improve the optoelectronic properties of OSCs and increase the carrier transport and PCE by reducing the interfacial resistance and enhancing efficient charge extraction.

In this study, both a ternary active layer and poly(9,9-bis(3′-(N,N-dimethyl)-N-ethylammoniumpropyl-2,7-fluorene)-alt-2,7-(9,9-dioctylfluorene)) dibromide (PFN-Br) were introduced to improve carrier transport and dissociation by controlling the interfacial resistance. The ternary active layer mainly extended the optoelectronic properties by introducing $PC_{71}BM$, which exhibits absorption properties in the short-

wavelength region into a binary active layer based on a non-fullerene acceptor, which absorbs in the long-wavelength region, to enhance carrier generation. The ternary active layer served to achieve vertical phase separation of the donor and acceptor, resulting in a decrease in interfacial resistance and improvement in carrier transport.[33] Furthermore, the intro-duction of the PFN-Br buffer layer improved the interfacial contact between the active layer and the ZnO layer used as ETL. These results induced the well-distributed vertical phase separation of the active layer to reduce the interfacial resistance. Consequently, the synergetic effects of the ternary active layer and PFN-Br effectively reduced the interfacial resistance of the OSCs and achieved a PCE of 13.2%.

2. EXPERIMENTAL SECTION

2.1. Materials. P(Cl−Cl) (BDD = 0.2) used as donor was synthesized with the same process as the previous literature.[34] Photoactive materials of 3,9-bis(2-methylene-((3-(1,1-dicyano-methylene)-6,7-difluoro)-indanone))-5,5,11,11-tetrakis(4-hexylphenyl)dithieno[2,3-d:2′,3′-d′]-s-indaceno[1,2-b:5,6-b′]-dithiophene (IT-4F, used as an acceptor) and $PC_{71}BM$ (used as an acceptor and third components) were purchased from 1-Materials (Canada) and Solarmer (China), respectively. Chlorobenzene (CB) and 1,8-diiodooctane (DIO) used as solvent and additives were purchased from Sigma-Aldrich (Germany). PFN-Br (PFN-P2) used as buffer layer was purchased from 1-Materials (Canada). ITO glass used as an electrode for OSCs was purchased from AMG (Republic of Korea).

2.2. Preparation of Solution. The solution of binary active layer was formed at 1:1 ratio of P(Cl−Cl) (BDD = 0.2) and IT-4F which dissolved in CB (DIO, 0.5% v/v) solution. The solution of ternary active layer was formed at various ratios from 1:1:0 to 1:0.7:0.3 and 1:0:1 of P(Cl−Cl) (BDD = 0.2), IT-4F, and $PC_{71}BM$ which dissolved in CB (DIO, 0.5% v/v) solution and was then used after stirring at 90 °C for 1 h. PFN-Br solution was prepared with concentration of 0.5 mg/mL in methanol.

2.3. Device Fabrication. To fabricate the inverted OSCs, patterned ITO glass was cleaned by ultrasonication using Alconox (neutral detergent), isopropyl alcohol (IPA), and deionized water (DI water). After these processes, UVO cleaning (Ahtech LTS AH 1700) was performed. After cleaning,the sol−gel derived ZnO precursor was spin-coated in ambient conditions and annealed at 200 °C to form the ETLs with thickness of 30 nm. Prepared PFN-Br solution was spin-coated onto ZnO layer with thickness of 5−20 nm in control devices. Prepared active solutions (binary and ternary) were spin-coated, and then the films were annealed at 140 °C for 10 min with a thickness of 80−100 nm in a N_2-filled glovebox. Finally, MoO_3 (5 nm) and Ag (100 nm) electrodes were formed through thermal evaporation with a high-vacuum chamber (under 1×10^{-6} Torr). The active areas of fabricated devices were 0.04 cm^2 and 1 cm^2.

2.4. Device Characterization. The current density−voltage (J−V) characteristics of fabricated OSCs were measured by a Keithely 2400 source measure unit and solar simulator (Oriel, AM 1.5G, 100 mW/cm^2). The incident photon-to-current conversion efficiency (IPCE) was measured to determine the external quantum efficiency (EQE) by using a Polarnix K3100 IPCE measurement system (Mc science). Absorption and emission properties were measured using ultraviolet−visible (UV−vis) spectrometer (Agilent 8453) and photoluminescence (PL) spectrometer (PerkinElmer, LS55), respec-tively. Interfacial resistance properties of fabricated OSCs were measured by using electrochemical impedance spectroscopy (EIS) under 1 sun illumination conditions (AM 1.5G, 100 mW/cm^2) applied at a frequency from 500 Hz to 1 MHz. Energy level alignment was analyzed via ultraviolet photoelectron spectroscopy (UPS) (AXIS-NOVA). Carrier transport properties calculated via the space charge limited current (SCLC) method with fabricating electron and hole only devices. Grazing incidence wide-angle X-ray scattering (GIWAXS) was measured to analyze crystalline structures of the
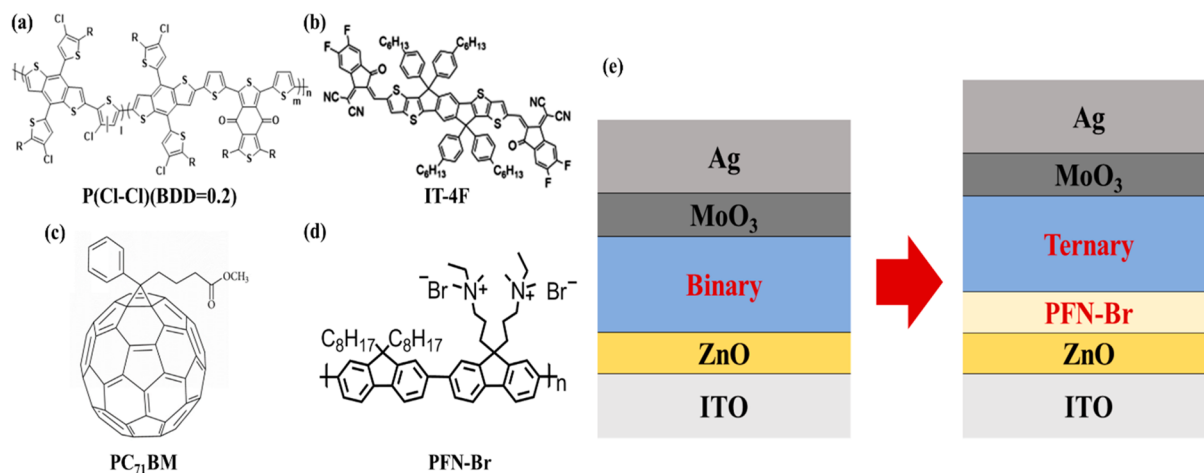
Figure 1. Structures of (a) P(Cl−Cl) (BDD = 0.2) used as donor, (b) IT-4F used as acceptor, (c) $PC_{71}BM$ used as third component, (d) PFN-Br as buffer layer, and (e) structures of fabricated devices (left: reference device; right: control device).

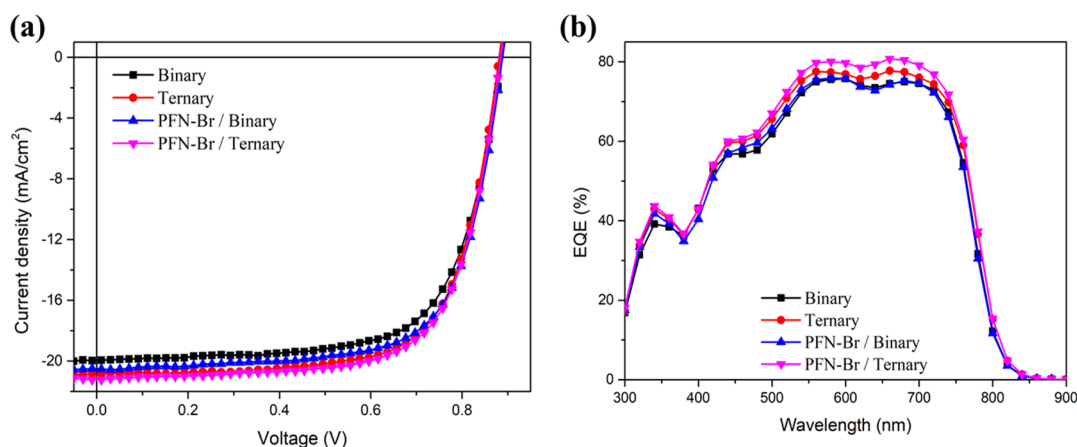**Figure 2.** (a) Current density−voltage (J−V) curve and (b) external quantum efficiency (EQE) characteristics of fabricated devices.

Table 1. Photovoltaic Properties of Fabricated Devices[a]

ETLs	active layer	V_{OC} (V)	J_{SC} (mA/cm^2)	FF (%)	PCE_{max}[b] (PCE_{ave})[b] (%)	R_S (Ω cm^2)	R_{Sh} (Ω cm^2)
ZnO	Binary[c]	0.878 (0.859 ± 0.02)	20.0 (19.9 ± 0.14)	69.1 (68.5 ± 0.57)	12.1 (11.9 ± 0.23)	5.8	998.0
	Ternary[d]	0.878 (0.859 ± 0.02)	20.9 (20.6 ± 0.31)	70.1 (69.8 ± 0.32)	12.8 (12.3 ± 0.49)	4.2	1251.4
ZnO/PFN-Br[e]	Binary[c]	0.878 (0.859 ± 0.02)	20.5 (20.4 ± 0.11)	70.3 (70.0 ± 0.27)	12.7 (12.4 ± 0.25)	4.6	1385.2
	Ternary[d]	0.878 (0.859 ± 0.02)	21.2 (21.1 ± 0.14)	70.7 (70.6 ± 0.11)	13.2 (13.0 ± 0.15)	3.9	1752.4

[a]The devices were fabricated into inverted structure (ITO/ZnO(PFN-Br)/BHJ layer/MoO$_3$/Ag, active area of 0.04 cm^2). [b]PCE_{max} is the maximum value, and PCE_{ave} are calculated values among 10 individual devices. [c]Optimized ratio of P(Cl−Cl) (BDD = 0.2) and IT-4F is 1:1. Optimized thickness of binary active layer is 100 nm with thermal annealing at 140 °C for 10 min. [d]Optimized ratio of P(Cl−Cl) (BDD = 0.2), IT-4F, and $PC_{71}BM$ is 1:0.9:0.1. Optimized thickness of ternary active layer is 100 nm with thermal annealing at 140 °C for 10 min. [e]Optimized thickness of PFN-Br is 10 nm.

formed film by using the 3C beamline at the Pohang Accelerator Laboratory (PAL). Atomic force microscopy (AFM) was measured to determine surface morphology analysis using a PSIA XE-100. Surface atomic profiles and cross-sectional analysis were measured by using field-emission scanning electron microscopy (FE-SEM) and the energy dispersive X-ray spectroscopy (EDS) mapping method.

3. RESULTS AND DISCUSSION

Figure 1 shows the structure of the materials and fabricated devices that were introduced into the devices fabricated in this study. The binary active layer based on P(Cl−Cl) (BDD = 0.2) (used as donor, Figure 1a), IT-4F (used as acceptor, Figure 1b), and the ternary active layer consisting of $PC_{71}BM$ (used as the third component, Figure 1c) that was introduced

into the binary active layer were incorporated into the device structure. In addition to the ternary layer, the conjugated polymer, PFN-Br (Figure 1d), was introduced between the ZnO (ETLs) and the active layer. Reference devices were fabricated by using an inverted structure (ITO/ZnO/active layer/MoO$_3$/Ag) (Figure 1e), and devices containing the ternary active layer and PFN-Br were introduced as control devices for comparison, either individually or together.

3.1. Photovoltaic Performance. Figure 2 and Table 1 present the current density−voltage (J−V) curve and external quantum efficiency (EQE) characteristics of the devices fabricated in this study. Specifically, the PCE of the device containing a ZnO/binary active layer (hereinafter termed
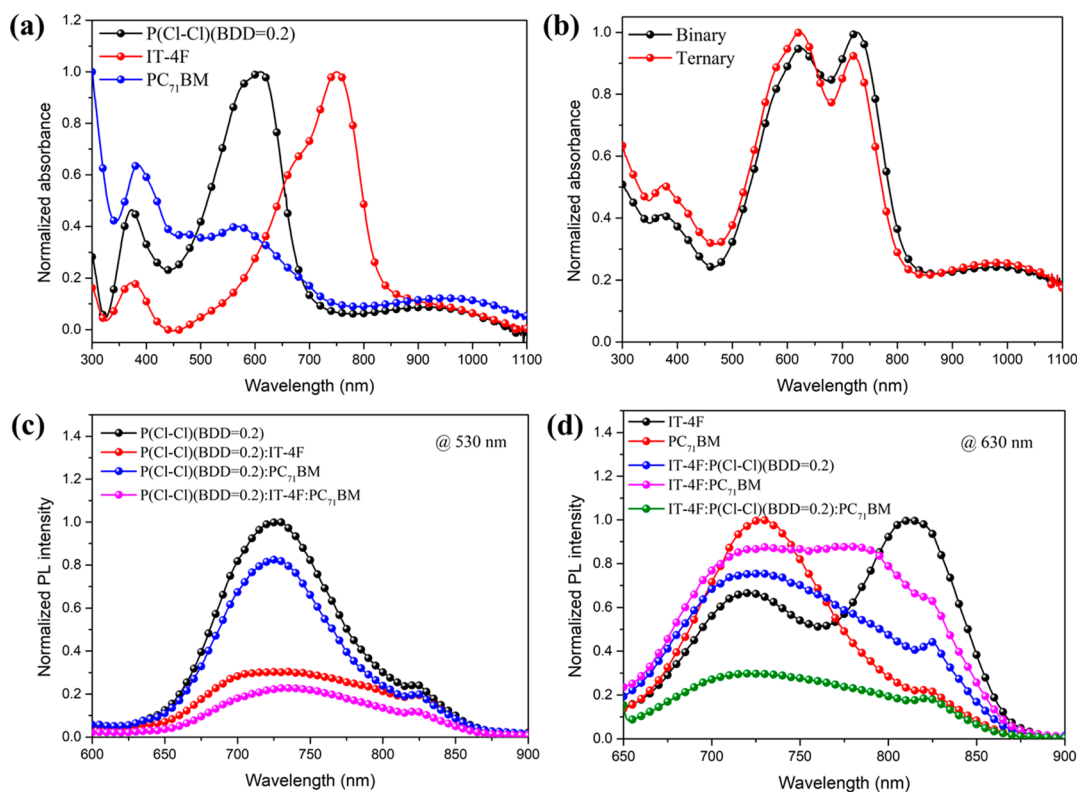
Figure 3. UV−vis absorption characteristics of (a) donor and acceptors, (b) binary active layer, ternary active layer, and PL spectra of pristine materials and optimized polymer blends: the samples were excited at (c) 530 nm and (d) 630 nm, respectively.

"Binary") was 12.1% (J_{SC} = 20.0 mA/cm^2, V_{OC} = 0.878 V, FF = 69.1%), whereas that of the device into which a ZnO/ternary active layer was introduced (hereinafter referred as "Ternary") was 12.8% (J_{SC} = 20.9 mA/cm^2, V_{OC} = 0.878 V, FF = 70.1%). Moreover, the PCE of the Binary device into which the PFN-Br was introduced (hereinafter termed "PFN-Br/Binary") was 12.7% (J_{SC} = 20.5 mA/cm^2, V_{OC} = 0.878 V, FF = 70.3%), and that of the Ternary device to which PFN-Br was introduced (hereinafter termed "PFN-Br/Ternary") was 13.2% (J_{SC} = 21.2 mA/cm^2, V_{OC} = 0.878 V, FF = 70.7%). The Ternary device improved both the J_{SC} (from 20.0 to 20.9 mA/cm^2) and FF (from 69.1 to 70.1%) in comparison with the Binary device. In a similar manner, the introduction of PFN-Br also enhanced both the J_{SC} (from 20.0 to 20.5 mA/cm^2) and FF (from 69.1 to 70.3%). As a result, the introduction of both the ternary layer and PFN-Br significantly improved both the J_{SC} and FF. This enhancement resulted from a decrease in the series resistance (R_S) as a consequence of introducing the ternary layer and PFN-Br (from 4.7 to 3.9 Ω cm^2). (The optimized performance of the Ternary and PFN-Br devices with respect to various concentrations and thicknesses are exhibited in Figures S1 and S2 as well as Tables S1 and S2). In the EQE characteristics (Figure 2b), the calculated J_{SC} values were measured as 17.44, 17.59, 17.49, and 18.16 mA/cm^2 for the Binary, Ternary, PFN-Br/Binary, and PFN-Br/Ternary devices, respectively.[35] As shown in Figure 2a, the introduction of the ternary layer and PFN-Br led to a significant increase in J_{SC}.

3.2. Optoelectronic Characteristics. Figure 3 shows the UV−vis absorption and photoluminescence (PL) properties of the fabricated devices. The absorption properties of P(Cl−Cl) (BDD = 0.2) as a donor were observed in the region of λ = 450−700 nm and for IT-4F as an acceptor in the region of λ =

500−850 nm. In contrast, the absorption properties of PC$_{71}$BM were observed in the region of λ = ∼750 nm, showing a particularly strong intensity at short wavelengths (Figure 3a). After the introduction of the ternary layer, the absorption properties increased in the short wavelength region because of the influence of PC$_{71}$BM (Figure 3b). This extension of the absorption range of the Ternary device increased the number of photogenerated carriers.[36]

The PL characteristics were analyzed to determine whether photoinduced carrier transport occurred among the components of the active layer.[34−38] Figure 3c shows the emission spectra measured at the region of λ = 600−900 nm with excitation at λ = 530 nm, which is the excitation peak of P(Cl−Cl) (BDD = 0.2). The intensity of this peak weakened after introduction of the acceptors. In particular, the introduction of IT-4F resulted in a high quenching rate, whereas the introduction of PC$_{71}$BM resulted in a low quenching rate. These were resulted from different performances due to most efficient carrier dissociation and transport which were occurred with IT-4F (shown in Figure S1 and Table S1). Furthermore, the introduction of both acceptors led to the highest quenching rate. These results suggest that carrier dissociation and transport occur from P(Cl−Cl) (BDD = 0.2) to IT-4F and PC$_{71}$BM and that the formation of the ternary layer resulted in the most effective carrier transport dynamics.[39]

Figure 3d shows the emission spectra at the region of λ = 600−900 nm with excitation at λ = 630 nm, which is the excitation peak of IT-4F. The introduction of P(Cl−Cl) (BDD = 0.2) and PC$_{71}$BM induced PL quenching. In this case, a low quenching rate was observed between IT-4F and PC$_{71}$BM, confirming the occurrence of carrier transport. Similar to the case represented in Figure 3c, the formation of the ternary
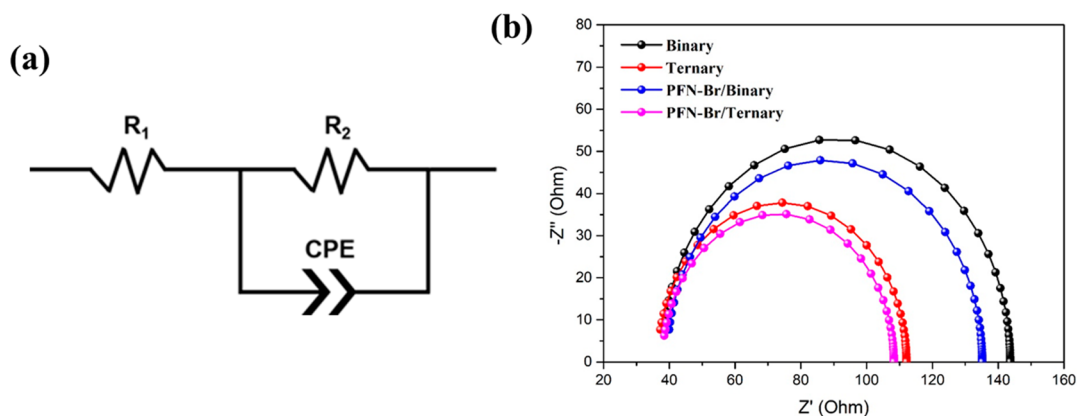
Figure 4. (a) Equivalent circuit employed in fitting impedance curves. (b) Nyquist plots of the cells with fabricated devices measured under 1 sun illumination.

layer shows the highest quenching rate, inducing effective carrier dissociation and transport. As a result, the formation of the ternary layer extended the absorption range, and the concomitant increase in the number of photogenerated carriers improved the J_{SC}. Moreover, the formation of the ternary layer effectively induced carrier dissociation and transport, thereby decreasing carrier recombination and thus contributing to the enhancement of FF.[40]

3.3. Electrochemical Characteristics. Figure S3 presents an analysis of the electronic characteristics and energy level alignment of devices after introduction of the ternary layer and PFN-Br using ultraviolet photoelectron spectroscopy (UPS). The levels of the highest occupied molecular orbitals (HOMO) (E_{HOMO}) and those of the conduction band (E_{CB}) of the active layer were calculated via the following equation, and the optical band gap (E_g) was calculated by using the onset peak of absorption properties.

$$E_{HOMO(CB)} = h\nu - (E_{cutoff} - E_{onset})$$

The onset peak of binary layer occurs at approximately $\lambda = 849$ nm, exhibiting $E_g = 1.46$ eV as well as the characteristics corresponding to $E_{cutoff} = 16.79$ eV, $E_{onset} = 1.70$ eV, $E_{HOMO} = -5.50$ eV, and $E_{LUMO} = -4.04$ eV. In contrast, the onset peak of ternary later occurs at approximately $\lambda = 873$ nm, exhibiting $E_g = 1.42$ eV as well as the characteristics corresponding to $E_{cutoff} = 16.71$ eV, $E_{onset} = 1.70$ eV, $E_{HOMO} = -5.57$ eV, and $E_{LUMO} = -4.15$ eV. Moreover, pristine ZnO exhibited the characteristics corresponding to $E_{cutoff} = 17.40$ eV, $E_{onset} = 3.70$ eV, and $E_{CB} = -3.82$ eV. However, ZnO/PFN-Br showed $E_{cutoff} = 17.69$ eV and $E_{onset} = 3.70$ eV, corresponding to $E_{CB} = -4.27$ eV. The energy level alignment is indicated on the basis of the calculated results (Figure S3c). These results confirmed the formation of a small energy barrier between the ITO electrode and ZnO/PFN-Br rather than pristine ZnO as well as the minimization of interfacial energy loss. These results suggest the availability of effective dissociation and transport of increased photogenerated carriers by ternary layer as well as carrier recombination control.[41] Consequently, the energy alignment resulting from the introduction of PFN-Br, which is favorable to carrier transport, contributed to the enhancement of J_{SC} and FF.

The dark $J-V$ curve shown in Figure S4 confirms these results. The introduction of the ternary and PFN-Br layers resulted in low leakage current density in the reverse bias region with determining lower carrier recombination.[42,43] Also,

to determine carrier dissociation and transport tendency, the photocurrent density−effective voltage ($J_{ph}-V_{eff}$) dependence were measured (shown in Figure S5). The $J_{ph}-V_{eff}$ dependence was calculated with $J_{ph} = J_L - J_D$ (where J_L is current density under light illumination and J_D is under dark conditions) and $V_{eff} = V_0 - V_{app}$ (where V_{app} is the applied voltage and V_0 is V_{app} when the current density is J_{ph}). The device introduced both of ternary and PFN-Br exhibited highest saturated J_{ph}, with a strong tendency of exciton generation and carrier dissociation.[44] These results indicate that the introduction of the ternary and PFN-Br layers induced efficient carrier dissociation and transport, thereby contributing to the enhancement of J_{SC} and FF, as is shown in Figure 3.

The observed enhancement of the J_{SC} and FF via carrier transport can be attributed to the internal change in interfacial resistance. This was examined by using electrochemical impedance spectroscopy (EIS) to measure the electrochemical characteristics. Figure 4 shows the equivalent circuit model and Nyquist plot for the fabricated OSCs under 1 sun illumination. In addition, the parameters that were employed to fit the impedance spectra are provided in Table 2. In the equivalent

Table 2. Parameters Employed for the Fitting of the Impedance Spectra by Use of an Equivalent Circuit Model[a]

ETLs	active layer	R_1 (Ω)	R_2 (Ω)	CPE-T	CPE-P
ZnO	Binary[b]	38.67	105.01	1.69×10^{-8}	0.984
	Ternary[c]	37.27	74.83	2.17×10^{-8}	0.986
ZnO/PFN-Br[d]	Binary[b]	39.94	95.22	2.12×10^{-8}	0.983
	Ternary[c]	38.49	69.79	2.26×10^{-8}	0.991

[a]The EIS analysis conducted with fabricated devices into inverted structure (ITO/ZnO/(PFN-Br)/BHJ layer/MoO3/Ag, active area of 0.04 cm²). [b]Optimized ratio of P(Cl−Cl)(BDD = 0.2) and IT-4F is 1:1. Optimized thickness of binary active layer is 100 nm with thermal annealing at 140 °C for 10 min. [c]Optimized ratio of P(Cl−Cl)(BDD = 0.2), IT-4F, and PC71BM is 1:0.9:0.1. Optimized thickness of ternary active layer is 100 nm with thermal annealing at 140 °C for 10 min. [d]Optimized thickness of PFN-Br is 10 nm.

circuit, constant phase element (CPE), CPE-T, and CPE-P refer to the nonideal behavior of the capacitor, applied amplitude, and the degree of ideal behavior, respectively. Specifically, as the value of CPE-P approaches 1, ideal capacitor behavior without defects becomes more prevalent.[45,46] In this case, the value of R_1 at high frequencies is
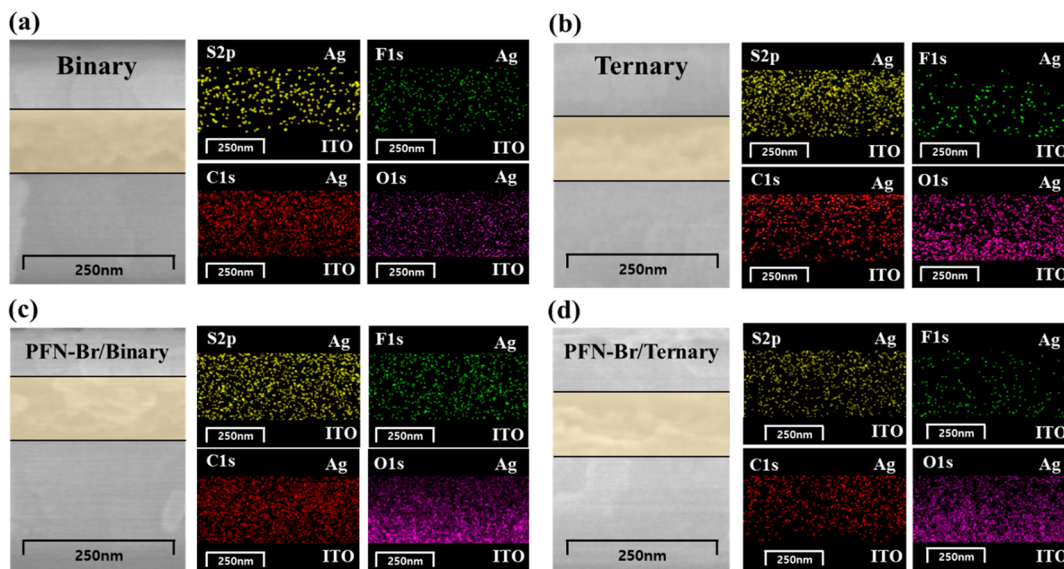
Figure 5. Cross-sectional field-emission scanning electron microscope (FE-SEM) image and energy dispersive X-ray spectra (EDS) mapping of each element in active layer: (a) Binary, (b) Ternary, (c) PFN-Br/Binary, and (d) PFN-Br/Ternary.

attributed mainly to the sheet resistance of ITO, also taking into account the contact resistance between the ITO and ZnO layer.[47] The electrochemical impedance spectrum was recorded at the V_{OC} in the frequency range of 500 Hz−1 MHz with an amplitude of 25 mV under 1 sun illumination. The Nyquist plot was constructed via a complex number plane composed of the real (Z') and imaginary (Z'') impedance components, according to the respective applied frequencies. The appearance of the same type of semicircle in this case indicates that the same process occurs at the interface.

All devices with the same ITO/ETLs (ZnO) interfacial structure showed similar R_1 values (38.67, 39.94, 37.27, and 38.49 Ω). Furthermore, R_2 refers to the carrier transport resistance, which corresponds to the sum of (1) the interfacial resistance between the donor and acceptor in the active layer and (2) the interfacial resistance between the active layer and ETLs.[48−50] The value of R_2 decreased more in the Binary device (R_2 = 105.01 Ω) than in the Ternary device (R_2 = 74.83 Ω) and was even lower because of the introduction of PFN-Br (R_2 = 95.22 Ω). Furthermore, the introduction of both the ternary layer and PFN-Br led to the lowest resistance (R_2 = 69.79 Ω) and exhibited ideal CPE-P (0.991).

Figure S6 shows the Nyquist plots of the devices measured under dark conditions. In this condition, the size of the EIS semicircle reflects the recombination resistance (R_{rec}). The high R_{rec} is consistent with the suppressed carrier recombination probabilities in OSCs.[51,52] The device introducing both of ternary and PFN-Br exhibited the highest R_{rec} which was consistent with highest shunt resistance (R_{Sh}) in Table 1. These results suggest that introduction of the ternary layer resulted in the reduction of the interfacial resistance between the donor and acceptor within the active layer and that the introduction of PFN-Br decreased the interfacial resistance between the active layer and the ZnO layer.

Figure S7 and Table S3 show the electron and hole mobilities, which were calculated by using the space carrier limited current (SCLC) method. For the purpose of this analysis, electron-only devices (ITO/ZnO/(PFN-Br)/active layer/LiF/Al) and hole-only devices (ITO/PEDOT:PSS/

active layer/MoO$_3$/Ag) were fabricated, and the calculations were performed by using the Mott−Gurney equation:[53]

$$J = (9/8)\varepsilon_r\varepsilon_0\mu_{eff}(V^2/L^3)$$

where J, ε_r, ε_0, μ_{eff}, V, and L refer to the current density, dielectric constant, free space permittivity, carrier mobility, applied voltage, and film thickness, respectively. The following values were calculated for the electron mobility (μ_e) and hole mobility (μ_h) of Binary and Ternary devices: $\mu_e = 2.78 \times 10^{-5}$ cm^2/(V s), $\mu_h = 1.11 \times 10^{-5}$ cm^2/(V s) and $\mu_e = 5.18 \times 10^{-5}$ cm^2/(V s), $\mu_h = 1.57 \times 10^{-5}$ cm^2/(V s), respectively. Moreover, the electron mobilities after the introduction of PFN-Br were calculated as $\mu_e = 3.05 \times 10^{-4}$ and 6.49×10^{-4} cm^2/(V s) for PFN-Br/Binary and PFN-Br/Ternary devices, respectively. As a result, the introduction of the ternary layer increased both the electron and hole mobilities, and the introduction of PFN-Br increased the electron mobility. Consequently, the introduction of both the ternary layer and PFN-Br resulted in improvements in the carrier transport properties by reducing the interfacial resistance on the interior and exterior of the active layer, thereby contributing to the enhancement in J_{SC} and FF.

3.4. Nanostructure and Morphological Characteristics. The reduction in interfacial resistance can be identified through the nanoscale phase control that occurs in the interior of the active layer as well as at the interface between the active layer and PFN-Br. Figure 5 shows the molecular behavior for the various device structures, which was analyzed using cross-sectional field-emission scanning electron microscopy (FE-SEM) and energy-dispersive X-ray spectroscopy (EDS) mapping.[54−56] To identify the distribution of P(Cl−Cl) (BDD = 0.2), IT-4F, and PC$_{71}$BM, visual images were obtained for the C 1s, O 1s, S 2p, and F 1s atomic signals by using EDS mapping. As shown for the molecular structures in Figures 1a−d, P (Cl−Cl) (BDD = 0.2) was analyzed by using the S 2p signals, which comprise a large portion of its molecular structure, and IT-4F was analyzed by using the characteristic F 1s atomic signal. P(Cl−Cl) (BDD = 0.2) exhibited a relatively low C/S ratio of 7.53, meaning high contents of S atoms, while IT-4F exhibited 23.5, meaning
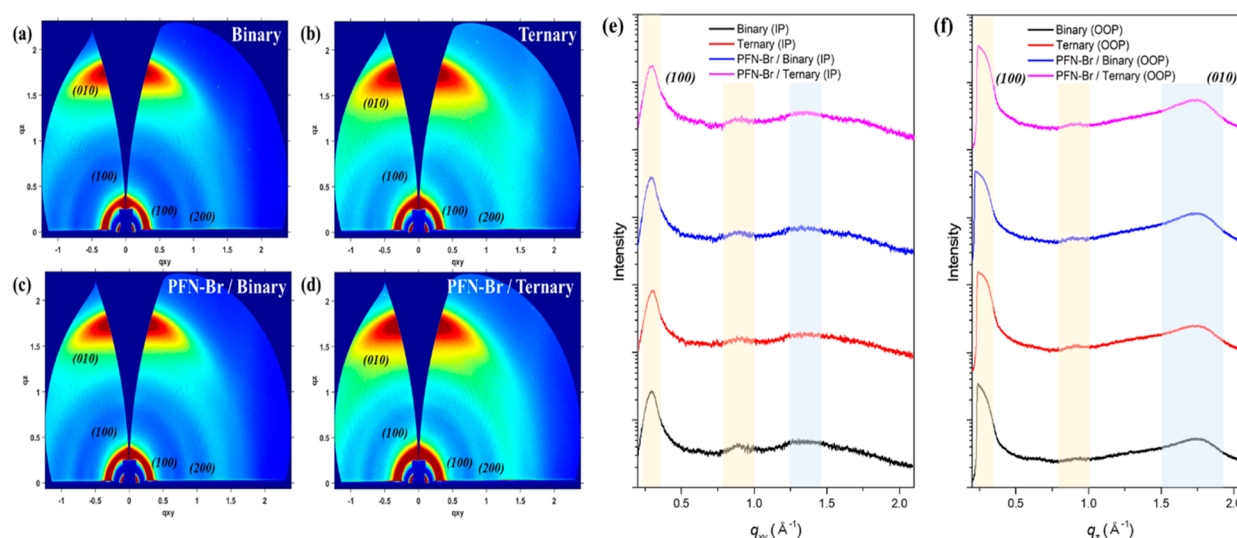
Figure 6. Crystalline structure measured by grazing incidence wide-angle X-ray scattering (GIWAXS) of formed active layer and ETL films: (a) Binary layer, (b) Ternary layer, (c) PFN-Br/Binary layer, and (d) PFN-Br/Ternary layer. Line-cut profiles for (e) in-plane (IP) direction and (f) out-of-plane (OOP) direction.

lower contents. Furthermore, $PC_{71}BM$ was analyzed by using the O 1s and C 1s signals. The mapping properties of the respective atomic signals were used to determine the behavior of the corresponding molecules in the active layer.[54]

The formation of the ternary layer by the addition of $PC_{71}BM$ resulted in a noticeable trend in the O 1s signals (Figure 5b). In this case, S 2p signals were prominent on the upper portion of the active layer, whereas the C 1s, O 1s, and F 1s signals were prominent on the lower portion. This result suggests that because of the introduction of $PC_{71}BM$, most P(Cl−Cl) (BDD = 0.2) is distributed across the upper portion of the active layer, and IT-4F and $PC_{71}BM$ are distributed across the lower portion, which corresponds to the behavior of vertical phase separation.[33]

Moreover, after the introduction of PFN-Br, the S 2p signals tended to be distributed across the upper portion of the active layer, whereas the C 1s, O 1s, and F 1s signals were distributed across the lower portion. The introduction of PFN-Br caused the properties of the ZnO surface to change, thereby improving the interfacial contact with the active layer.[57,58] As a result, the introduction of both the ternary layer and PFN-Br resulted in the formation of well-dispersed vertical phase separation, exhibiting both of the aforementioned trends of the two strategies.

We also characterized cross-sectional depth-profiling characteristics through time-of-flight secondary ion mass spectrometry (TOF-SIMS) analysis for deeper understanding of vertical phase separation (shown in Figure S8). In depth profiling, the Cl ionic signals from P(Cl−Cl) (BDD = 0.2) mainly distributed at the top of photoactive layer. However, the F ionic signals from IT-4F were distributed across the photoactive layer, but they exhibited a bottom dominant tendency. The O ionic signals also exhibited a bottom dominant tendency. These O ionic signals mainly resulted from $PC_{71}BM$ exhibiting different tendency with F and Cl ionic signals. With ternary and PFN-Br, the Cl ionic signals moved toward the top of the photoactive layer, while the F and O ionic signals distributed toward the bottom layer. These results are consistent with the behavior of vertical phase separation.[32]

Figure 6 shows the crystalline structures and line-cut profiles of the formed active layer and ETLs films measured by grazing incidence wide-angle X-ray scattering (GIWAXS). All films composed of P(Cl−Cl) (BDD = 0.2) and IT-4F exhibited obvious face-on dominant crystalline structure with a large (010) peak around q_z = 1.75 Å^{-1} with ∼0.36 nm of π−π stacking distance (d_{010}) and, furthermore, a high (100) peak around q_{xy} = 0.29 Å^{-1} with ∼2.17 nm of lamellar stacking distance (d_{100}). After addition of $PC_{71}BM$, the ternary layer exhibited an amorphous ring peak and slightly shifted (010) peak around q_z = 1.77 Å^{-1} with ∼0.35nm, which means more close-packed molecular stacking. Also, the ternary layer exhibited a high-intensity (010) peak with enhanced π−π stacking resulting from vertical phase separation (in Figure 6b). After addition of PFN-Br, the film exhibited slightly enhanced face-on crystalline structure resulting from a well-distributed molecular formation (in Figure 6c). Finally, by the synergetic effects of ternary layer and PFN-Br, the formed film exhibited highest close-packed and well-ordered molecular stacking. These results could be obtained because $PC_{71}BM$, having a relatively high surface energy within the ternary active layer, accumulated in the PFN-Br layer by way of rearrangement during the film-formation process.[33] The introduction of the ternary layer and PFN-Br formed a well-dispersed vertical phase that favors carrier transport, resulting in the effective control of carrier recombination and thus contributing to the enhancement of J_{SC} and FF.[59−61]

Figures S9 and S10 show the morphological characteristics of the formed active layer and ETL films, which were analyzed by using atomic force microscopy (AFM) and FE-SEM top scanning. The root-mean-square roughness (R_q) properties were determined to be 1.427 and 1.319 nm for the binary and ternary layer films, respectively, resulting in the formation of a uniform morphology and fine domains in ternary layer. In addition, a binary layer with the introduction of PFN-Br resulted in a more uniform morphology $(R_q = 1.267$ nm) because of the improved interfacial contact. These results were obtained because of the change in the morphological characteristics resulting from the introduction of PFN-Br as well as from the change in the surface properties (Figure
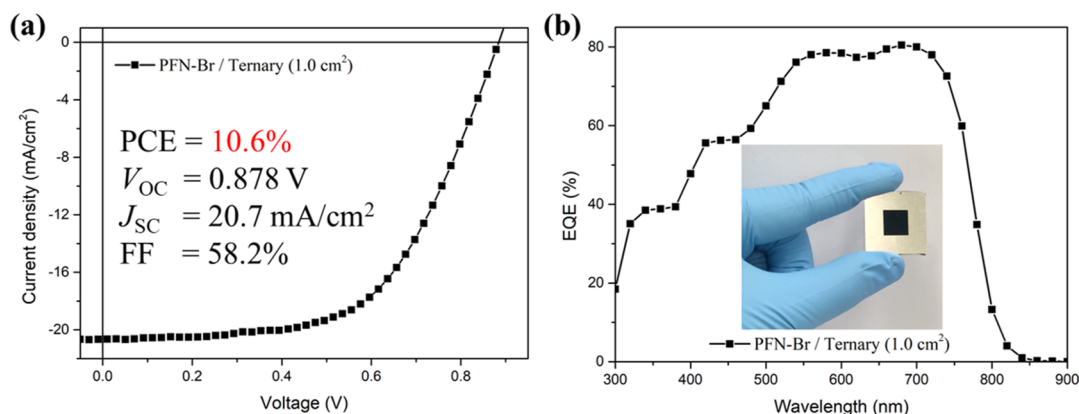
Figure 7. (a) $J-V$ characteristics and (b) EQE characteristics of fabricated large-area devices introducing Ternary and PFN-Br strategy in an active area of 1.0 cm^2.

S9c,d). Furthermore, the introduction of the ternary layer and PFN-Br resulted in the most uniform morphology (R_q = 1.245 nm) and the densest film (Figures S9f and S10d). These uniform and dense morphological characteristics reduced the interfacial resistance and then increased the effective carrier transport.

The strategies involving the introduction of the ternary layer and PFN-Br were expanded by successfully fabricating a large-area device (with an active area of 1.0 cm^2) via spin-coating (in Figure 7). The fabricated large-area device exhibited a PCE of 10.6% (V_{OC} = 0.878 V, J_{SC} = 20.7 mA/cm^2, and FF = 58.2%) and high EQE characteristics in excess of 80% in the λ = 550–800 nm region, indicating efficient carrier dissociation and transport as a result of the decreased interfacial resistance.

4. CONCLUSION

This study aimed to introduce a ternary active layer and conjugated polymer to reduce the interfacial resistance in both the interior and on the exterior of the active layer and further enhance carrier transport. PC$_{71}$BM was introduced into a device with a binary active layer based on P(Cl–Cl) (BDD = 0.2) and IT-4F to form a ternary active layer. In this case, the ternary active layer was extended of optical properties and induced vertical phase separation in the active layer to reduce the interfacial resistance between the donor and the acceptor. Moreover, the conjugated polymer, PFN-Br, was introduced between the active layer and ZnO (ETLs) with the aim of controlling the surface properties, and the formation of a well-dispersed vertical phase reduced the interfacial resistance between the active layer and ETLs. The introduction of the ternary layer and PFN-Br enabled the formation of a phase in which efficient carrier dissociation and transport were both realized, thereby successfully reducing the interfacial resistance. Consequently, the significant increase in J_{SC} and FF resulted in a high PCE of 13.2%. The reduction in the interfacial resistance of OSCs is of key importance for high performance, and the results from in-depth studies such as this one could be applied to flexible and large-area devices.

ASSOCIATED CONTENT

ⓈⒾ Supporting Information

The Supporting Information is available free of charge at https://pubs.acs.org/doi/10.1021/acsaem.0c00218.

Experimental data of $J-V$ (dark $J-V$) curve, $J_{ph}-V_{eff}$, dark EIS, UPS, SCLC, TOF-SIMS, AFM, and FE-SEM measurements (PDF)

AUTHOR INFORMATION

Corresponding Author

Doo Kyung Moon − *Nano and Information Materials Lab. (NIMs Lab.), Department of Chemical Engineering, Konkuk University, Seoul 05029, Republic of Korea;* ⓘ orcid.org/0000-0001-9482-7508; Phone: +82-2-450-3498; Email: dkmoon@konkuk.ac.kr; Fax: +82-2-444-0765

Authors

Hee Seon Park − *Nano and Information Materials Lab. (NIMs Lab.), Department of Chemical Engineering, Konkuk University, Seoul 05029, Republic of Korea*

Yong Woon Han − *Nano and Information Materials Lab. (NIMs Lab.), Department of Chemical Engineering, Konkuk University, Seoul 05029, Republic of Korea*

Hyoung Seok Lee − *Nano and Information Materials Lab. (NIMs Lab.), Department of Chemical Engineering, Konkuk University, Seoul 05029, Republic of Korea*

Sung Jae Jeon − *Nano and Information Materials Lab. (NIMs Lab.), Department of Chemical Engineering, Konkuk University, Seoul 05029, Republic of Korea*

Complete contact information is available at:
https://pubs.acs.org/10.1021/acsaem.0c00218

Notes

The authors declare no competing financial interest.

REFERENCES

(1) Li, G.; Zhu, R.; Yang, Y. Polymer Solar Cells. *Nat. Photonics* **2012**, *6* (3), 153−161.

(2) Shrotriya, V. Organic Photovoltaics: Polymer Power. *Nat. Photonics* **2009**, *3* (8), 447−449.

(3) Cui, Y.; Yao, H.; Zhang, J.; Zhang, T.; Wang, Y.; Hong, L.; Xian, K.; Xu, B.; Zhang, S.; Peng, J.; Wei, Z.; Gao, F.; Hou, J. Over 16% Efficiency Organic Photovoltaic Cells Enabled by a Chlorinated Acceptor with Increased Open-Circuit Voltages. *Nat. Commun.* **2019**, *10* (1), 2515−2522.

(4) Lin, Y.; Adilbekova, B.; Firdaus, Y.; Yengel, E.; Faber, H.; Sajjad, M.; Zheng, X.; Yarali, E.; Seitkhan, A.; Bakr, O. M.; et al. 17% Efficient Organic Solar Cells Based on Liquid Exfoliated WS2 as a Replacement for PEDOT:PSS. *Adv. Mater.* **2019**, *31* (46), 1902965.

(5) Su, Y. W.; Lan, S. C.; Wei, K. H. Organic Photovoltaics. *Mater. Today* **2012**, *15* (12), 554−562.

(6) Han, Y. W.; Jeon, S. J.; Lee, H. S.; Park, H.; Kim, K. S.; Lee, H. W.; Moon, D. K. Evaporation-Free Nonfullerene Flexible Organic Solar Cell Modules Manufactured by An All-Solution Process. *Adv. Energy Mater.* **2019**, *9* (42), 1902065.

(7) Søndergaard, R.; Hösel, M.; Angmo, D.; Larsen-Olsen, T. T.; Krebs, F. C. Roll-to-Roll Fabrication of Polymer Solar Cells. *Mater. Today* **2012**, *15* (1−2), 36−49.

(8) Espinosa, N.; García-Valverde, R.; Urbina, A.; Krebs, F. C. A Life Cycle Analysis of Polymer Solar Cell Modules Prepared Using Roll-to-Roll Methods under Ambient Conditions. *Sol. Energy Mater. Sol. Cells* **2011**, *95* (5), 1293−1302.

(9) Meng, X.; Zhang, L.; Xie, Y.; Hu, X.; Xing, Z.; Huang, Z.; Liu, C.; Tan, L.; Zhou, W.; Sun, Y.; Ma, W.; Chen, Y. A General Approach for Lab-to-Manufacturing Translation on Flexible Organic Solar Cells. *Adv. Mater.* **2019**, *31* (41), 1903649.

(10) Zhang, Y.-X.; Fang, J.; Li, W.; Shen, Y.; Chen, J.-D.; Li, Y.; Gu, H.; Pelivani, S.; Zhang, M.; Li, Y.; Tang, J.-X. Synergetic Transparent Electrode Architecture for Efficient Non-Fullerene Flexible Organic Solar Cells with > 12% Efficiency. *ACS Nano* **2019**, *13* (4), 4686−4694.

(11) Lei, T.; Peng, R.; Song, W.; Hong, L.; Huang, J.; Fei, N.; Ge, Z. Bendable and Foldable Flexible Organic Solar Cells Based on Ag Nanowire Films with 10.30% Efficiency. *J. Mater. Chem. A* **2019**, *7* (8), 3737−3744.

(12) Jeon, S. J.; Han, Y. W.; Moon, D. K. Drastic Changes in Properties of Donor-Acceptor Polymers Induced by Asymmetric Structural Isomers for Application to Polymer Solar Cells. *ACS Appl. Mater. Interfaces* **2019**, *11* (9), 9239−9250.

(13) Yu, J. E.; Jeon, S. J.; Choi, J. Y.; Han, Y. W.; Ko, E. J.; Moon, D. K. A 3-Fluoro-4-Hexylthiophene-Based Wide Bandgap Donor Polymer for 10.9% Efficiency Eco-Friendly Nonfullerene Organic Solar Cells. *Small* **2019**, *15* (9), 1805321.

(14) Lee, Y. J.; Jeon, S. J.; Choi, J. Y.; Moon, D. K. Design and Synthesis of Acceptor−donor−acceptor Small Molecule Based on Caffeine Derivative for Efficient and Stable Polymer Solar Cells. *J. Ind. Eng. Chem.* **2019**, *75*, 138−147.

(15) Ye, L.; Xiong, Y.; Chen, Z.; Zhang, Q.; Fei, Z.; Henry, R.; Heeney, M.; O'Connor, B. T.; You, W.; Ade, H. Sequential Deposition of Organic Films with Eco-Compatible Solvents Improves Performance and Enables Over 12%-Efficiency Nonfullerene Solar Cells. *Adv. Mater.* **2019**, *31* (17), 1808153.

(16) Li, H.; Xiao, Z.; Ding, L.; Wang, J. Thermostable Single-Junction Organic Solar Cells with a Power Conversion Efficiency of 14.62%. *Sci. Bull.* **2018**, *63* (6), 340−342.

(17) Zhang, Y.; Feng, H.; Meng, L.; Wang, Y.; Chang, M.; Li, S.; Guo, Z.; Li, C.; Zheng, N.; Xie, Z.; Wan, X.; Chen, Y. High Performance Thick-Film Nonfullerene Organic Solar Cells with Efficiency over 10% and Active Layer Thickness of 600 nm. *Adv. Energy Mater.* **2019**, *9* (45), 1902688.

(18) Garcia-Belmonte, G.; Boix, P. P.; Bisquert, J.; Sessolo, M.; Bolink, H. J. Simultaneous Determination of Carrier Lifetime and Electron Density-of-States in P3HT:PCBM Organic Solar Cells under Illumination by Impedance Spectroscopy. *Sol. Energy Mater. Sol. Cells* **2010**, *94* (2), 366−375.

(19) Kuwabara, T.; Iwata, C.; Yamaguchi, T.; Takahashi, K. Mechanistic Insights into UV-Induced Electron Transfer from PCBM to Titanium Oxide in Inverted-Type Organic Thin Film Solar Cells Using AC Impedance Spectroscopy. *ACS Appl. Mater. Interfaces* **2010**, *2* (8), 2254−2260.

(20) Glatthaar, M.; Riede, M.; Keegan, N.; Sylvester-Hvid, K.; Zimmermann, B.; Niggemann, M.; Hinsch, A.; Gombert, A. Efficiency Limiting Factors of Organic Bulk Heterojunction Solar Cells Identified by Electrical Impedance Spectroscopy. *Sol. Energy Mater. Sol. Cells* **2007**, *91* (5), 390−393.

(21) Pan, M. A.; Lau, T. K.; Tang, Y.; Wu, Y. C.; Liu, T.; Li, K.; Chen, M. C.; Lu, X.; Ma, W.; Zhan, C. 16.7%-Efficiency Ternary Blended Organic Photovoltaic Cells with PCBM as the Acceptor Additive to Increase the Open-Circuit Voltage and Phase Purity. *J. Mater. Chem. A* **2019**, *7* (36), 20713−20722.

(22) Hadmojo, W. T.; Wibowo, F. T. A.; Lee, W.; Jang, H.-K.; Kim, Y.; Sinaga, S.; Park, M.; Ju, S.-Y.; Ryu, D. Y.; Jung, I. H.; Jang, S.-Y. Performance Optimization of Parallel-Like Ternary Organic Solar Cells through Simultaneous Improvement in Charge Generation and Transport. *Adv. Funct. Mater.* **2019**, *29* (14), 1808731.

(23) Su, M. S.; Kuo, C. Y.; Yuan, M. C.; Jeng, U. S.; Su, C. J.; Wei, K. H. Improving Device Efficiency of Polymer/Fullerene Bulk Heterojunction Solar Cells through Enhanced Crystallinity and Reduced Grain Boundaries Induced by Solvent Additives. *Adv. Mater.* **2011**, *23* (29), 3315−3319.

(24) Liu, C. M.; Su, Y. W.; Jiang, J. M.; Chen, H. C.; Lin, S. W.; Su, C. J.; Jeng, U. S.; Wei, K. H. Complementary Solvent Additives Tune the Orientation of Polymer Lamellae, Reduce the Sizes of Aggregated Fullerene Domains, and Enhance the Performance of Bulk Heterojunction Solar Cells. *J. Mater. Chem. A* **2014**, *2* (48), 20760−20769.

(25) Lee, E. J.; Heo, S. W.; Han, Y. W.; Moon, D. K. An Organic-Inorganic Hybrid Interlayer for Improved Electron Extraction in Inverted Polymer Solar Cells. *J. Mater. Chem. C* **2016**, *4* (13), 2463−2469.

(26) Kuwabara, T.; Kawahara, Y.; Yamaguchi, T.; Takahashi, K. Characterization of Inverted-Type Organic Solar Cells with a ZnO Layer as the Electron Collection Electrode by Ac Impedance Spectroscopy. *ACS Appl. Mater. Interfaces* **2009**, *1* (10), 2107−2110.

(27) Khlyabich, P. P.; Rudenko, A. E.; Street, R. A.; Thompson, B. C. Influence of Polymer Compatibility on the Open-Circuit Voltage in Ternary Blend Bulk Heterojunction Solar Cells. *ACS Appl. Mater. Interfaces* **2014**, *6* (13), 9913−9919.

(28) Liu, T.; Huo, L.; Sun, X.; Fan, B.; Cai, Y.; Kim, T.; Kim, J. Y.; Choi, H.; Sun, Y. Ternary Organic Solar Cells Based on Two Highly Efficient Polymer Donors with Enhanced Power Conversion Efficiency. *Adv. Energy Mater.* **2016**, *6* (6), 1502109.

(29) Tran, V. H.; Khan, R.; Lee, I. H.; Lee, S. H. Low-Temperature Solution-Processed Ionic Liquid Modified SnO_2 as an Excellent Electron Transport Layer for Inverted Organic Solar Cells. *Sol. Energy Mater. Sol. Cells* **2018**, *179*, 260−269.

(30) Guo, J.; Ren, G.; Han, W.; Sun, Y.; Wang, M.; Zhou, Y.; Shen, L.; Guo, W. Facilitating Electron Extraction of Inverted Polymer Solar Cells by Using Organic/Inorganic/Organic Composite Buffer Layer. *Org. Electron.* **2019**, *68*, 187−192.

(31) Liu, C. M.; Su, M. S.; Jiang, J. M.; Su, Y. W.; Su, C. J.; Chen, C. Y.; Tsao, C. S.; Wei, K. H. Distribution of Crystalline Polymer and Fullerene Clusters in Both Horizontal and Vertical Directions of High-Efficiency Bulk Heterojunction Solar Cells. *ACS Appl. Mater. Interfaces* **2013**, *5* (12), 5413−5422.

(32) Cheng, H. W.; Raghunath, P.; Wang, K. L.; Cheng, P.; Haung, T.; Wu, Q.; Yuan, J.; Lin, Y. C.; Wang, H. C.; Zou, Y.; et al. Potassium-Presenting Zinc Oxide Surfaces Induce Vertical Phase Separation in Fullerene-Free Organic Photovoltaics. *Nano Lett.* **2020**, *20*, 715−721.

(33) Han, Y. W.; Choi, J. Y.; Lee, Y. J.; Ko, E. J.; Choi, M. H.; Suh, I. S.; Moon, D. K. Vertical Phase Separation for Highly Efficient Organic Solar Cells Incorporating Conjugated-Polyelectrolytes. *Adv. Mater. Interfaces* **2019**, *6*, 1801396.

(34) Jeon, S. J.; Han, Y. W.; Moon, D. K. 13.9%-Efficiency and Eco-Friendly Nonfullerene Polymer Solar Cells Obtained by Balancing

Molecular Weight and Solubility in Chlorinated Thiophene-Based Polymer Backbones. *Small* **2019**, *15* (41), 1902598.

(35) Kim, Y. H.; Sylvianti, N.; Marsya, M. A.; Park, J.; Kang, Y.; Moon, D. K.; Kim, J. H. A Simple Approach to Fabricate an E Ffi Cient Inverted Polymer Solar Cell with a Novel Small Molecular Electrolyte as the Cathode Bu Ff Er Layer. *ACS Appl. Mater. Interfaces* **2016**, *8*, 32992−32997.

(36) Fang, J.; Deng, D.; Zhang, J.; Zhang, Y.; Lu, K.; Wei, Z. High Open-Circuit Voltage Ternary Organic Solar Cells Based on ICBA as Acceptor and Absorption-Complementary Donors. *Mater. Chem. Front.* **2017**, *1* (6), 1223−1228.

(37) Ltaief, A.; Davenas, J.; Bouazizi, A.; Chaâbane, R. B.; Alcouffe, P.; Ouada, H. B. Film Morphology Effects on the Electrical and Optical Properties of Bulk Heterojunction Organic Solar Cells Based on MEH-PPV/C60 Composite. *Mater. Sci. Eng., C* **2005**, *25* (1), 67−75.

(38) Chen, X.-W.; Tao, S.-L.; Fan, C.; Chen, D.-C.; Zhou, L.; Lin, H.; Zheng, C.-J.; Su, S.-J. Ternary Organic Solar Cells with Coumarin7 as the Donor Exhibiting Greater Than 10% Power Conversion Efficiency and a High Fill Factor of 75%. *ACS Appl. Mater. Interfaces* **2017**, *9*, 29907−29916.

(39) Han, Y. W.; Lee, E. J.; Joo, J.; Park, J.; Sung, T. H.; Moon, D. K. Photon Energy Transfer by Quantum Dots in Organic−inorganic Hybrid Solar Cells through FRET. *J. Mater. Chem. A* **2016**, *4* (27), 10444−10453.

(40) Chen, Y.; Yang, L.; Wu, J.; Wang, G.; Huang, W.; Melkonyan, F. S.; Lu, Z.; Huang, Y.; Marks, T. J.; Facchetti, A. Performance, Morphology, and Charge Recombination Correlations in Ternary Squaraine Solar Cells. *Chem. Mater.* **2018**, *30* (19), 6810−6820.

(41) Upama, M. B.; Elumalai, N. K.; Mahmud, M. A.; Xu, C.; Wang, D.; Wright, M.; Uddin, A. Enhanced Electron Transport Enables over 12% Efficiency by Interface Engineering of Non-Fullerene Organic Solar Cells. *Sol. Energy Mater. Sol. Cells* **2018**, *187*, 273−282.

(42) Kang, R.; Oh, S. H.; Na, S. I.; Kim, T. S.; Kim, D. Y. Investigation into the Effect of Post-Annealing on Inverted Polymer Solar Cells. *Sol. Energy Mater. Sol. Cells* **2014**, *120*, 131−135.

(43) Duan, L.; Yi, H.; Xu, C.; Upama, M. B.; Mahmud, M. A.; Wang, D.; Shabab, F. H.; Uddin, A. Relationship between the Diode Ideality Factor and the Carrier Recombination Resistance in Organic Solar Cells. *IEEE J. Photovoltaics* **2018**, *8* (6), 1701−1709.

(44) Chen, M.; Zhang, Z.; Li, W.; Cai, J.; Yu, J.; Spooner, E. L. K.; Kilbride, R. C.; Li, D.; Du, B.; Gurney, R. S.; et al. Regulating the Morphology of Fluorinated Non-Fullerene Acceptor and Polymer Donor via Binary Solvent Mixture for High Efficiency Polymer Solar Cells. *Sci. China: Chem.* **2019**, *62* (9), 1221−1229.

(45) Zhang, Y.; Li, L.; Yuan, S.; Li, G.; Zhang, W. Electrical Properties of the Interfaces in Bulk Heterojunction Organicsolar Cells Investigated by Electrochemical Impedance Spectroscopy. *Electrochim. Acta* **2013**, *109*, 221−225.

(46) Jin, M. J.; Jo, J.; Yoo, J. W. Impedance Spectroscopy Analysis on the Effects of TiO$_2$ Interfacial Atomic Layers in ZnO Nanorod Polymer Solar Cells: Effects of Interfacial Charge Extraction on Diffusion and Recombination. *Org. Electron.* **2015**, *19*, 83−91.

(47) Koide, N.; Islam, A.; Chiba, Y.; Han, L. Improvement of Efficiency of Dye-Sensitized Solar Cells Based on Analysis of Equivalent Circuit. *J. Photochem. Photobiol., A* **2006**, *182* (3), 296−305.

(48) Xu, X.; Liu, Z.; Zuo, Z.; Zhang, M.; Zhao, Z.; Shen, Y.; Zhou, H.; Chen, Q.; Yang, Y.; Wang, M. Hole Selective NiO Contact for Efficient Perovskite Solar Cells with Carbon Electrode. *Nano Lett.* **2015**, *15* (4), 2402−2408.

(49) Hou, Y.; Yang, J.; Jiang, Q.; Li, W.; Zhou, Z.; Li, X.; Zhou, S. Enhancement of Photovoltaic Performance of Perovskite Solar Cells by Modification of the Interface between the Perovskite and Mesoporous TiO$_2$ Film. *Sol. Energy Mater. Sol. Cells* **2016**, *155*, 101−107.

(50) Chauhan, A. K.; Gusain, A.; Jha, P.; Veerender, P.; Koiry, S. P.; Sridevi, C.; Aswal, D. K.; Gupta, S. K.; Taguchi, D.; Manaka, T.; Iwamoto, M. Interfacial Charge Trapping in the Polymer Solar Cells and Its Elimination by Solvent Annealing. *AIP Adv.* **2016**, *6* (9), No. 095012.

(51) Liu, Z.; Liu, K.; Wang, H.; Jain, S. M.; Duan, J.; He, T.; Fan, R.; Yang, J.; Liu, H.; Zhang, F. Solvent Engineering Approach via Introducing Poly (3, 4-Ethylene Dioxy-Thiophene)−Poly (Styrene Sulfonate) (PEDOT:PSS) into Photosensitive Absorber Layer for Ambient Temperature Processed Efficient Inverted Planar Perovskite Solar Cells. *Sol. Energy* **2018**, *176*, 1−9.

(52) Jin, H. C.; Salma, S. A.; Moon, D. K.; Kim, J. H. Effect of Conjugated Polymer Electrolyte with Diverse Acid Derivatives as the Cathode Buffer Layer on the Photovoltaic Properties. *J. Mater. Chem. A* **2020**, *8*, 4562−4569.

(53) Zhang, Y.; Wang, H.; Xiao, Y.; Wang, L.; Shi, D.; Cheng, C. Liquid Crystalline Perylene Diimide Outperforming Nonliquid Crystalline Counterpart: Higher Power Conversion Efficiencies (PCEs) in Bulk Heterojunction (BHJ) Cells and Higher Electron Mobility in Space Charge Limited Current (SCLC) Devices. *ACS Appl. Mater. Interfaces* **2013**, *5* (21), 11093−11100.

(54) Choi, J. Y.; Han, Y. W.; Jeon, S. J.; Ko, E. J.; Moon, D. K. Introduction of Co-Additives to Form Well Dispersed Photoactive Layer to Improve Performance and Stability of Organic Solar Cells. *Sol. Energy* **2019**, *185*, 1−12.

(55) Pelicano, C. M.; Yanagi, H. Efficient Solid-State Perovskite Solar Cells Based on Nanostructured Zinc Oxide Designed by Strategic Low Temperature Water Oxidation. *J. Mater. Chem. C* **2017**, *5* (32), 8059−8070.

(56) Tian, H. Solid-State p-Type Dye-Sensitized Solar Cells: Progress, Potential Applications and Challenges. *Sustain. Energy Fuels* **2019**, *3* (4), 888−898.

(57) Liu, X.; Chen, Z.; Xu, R.; Zhang, R.; Hu, Z.; Huang, F.; Cao, Y. Finely Tuned Composition in Conjugated Polyelectrolytes for Interfacial Engineering of Efficient Polymer Solar Cells. *Small methods* **2018**, *2*, 1700407.

(58) Yang, T.; Wang, M.; Duan, C.; Hu, X.; Huang, L.; Peng, J.; Huang, F.; Gong, X. Inverted Polymer Solar Cells with 8.4% Efficiency by Conjugated Polyelectrolyte. *Energy Environ. Sci.* **2012**, *5* (8), 8208−8214.

(59) Kang, H.; Lee, J.; Jung, S.; Yu, K.; Kwon, S.; Hong, S.; Kee, S.; Lee, S.; Kim, D.; Lee, K. Self-Assembly of Interfacial and Photoactive Layers via One-Step Solution Processing for Efficient Inverted Organic Solar Cells. *Nanoscale* **2013**, *5* (23), 11587−11591.

(60) Bi, P.; Xiao, T.; Yang, X.; Niu, M.; Wen, Z.; Zhang, K.; Qin, W.; So, S. K.; Lu, G.; Hao, X.; Liu, H. Regulating the Vertical Phase Distribution by Fullerene-Derivative in High Performance Ternary Organic Solar Cells. *Nano Energy* **2018**, *46*, 81−90.

(61) Cui, Y.; Zhang, S.; Liang, N.; Kong, J.; Yang, C.; Yao, H.; Ma, L.; Hou, J. Toward Efficient Polymer Solar Cells Processed by Solution-Processed Layer-by-Layer Approach. *Adv. Mater.* **2018**, *30* (34), 1802499.